Erosion of archaeological sites

Huisman, Hans; De Kort, Jan-Willem; Ketterer, Michael E.; Reimann, Tony; Schoorl, Jeroen M.; van der Heiden, Menno; van Soest, Maud; van Egmond, Fenny

Published in:
Geoarchaeology

DOI:
10.1002/gea.21716

Publication date:
2019

Received: 22 December 2017 | Revised: 17 August 2018 | Accepted: 6 September 2018

DOI: 10.1002/gea.21716

RESEARCH ARTICLE

WILEY Geoarchaeology An International Journal

Erosion of archaeological sites: Quantifying the threat using optically stimulated luminescence and fallout isotopes

Hans Huisman[1,2] | Jan-Willem de Kort[1] | Michael E. Ketterer[3] | Tony Reimann[4] | Jeroen M. Schoorl[5] | Menno van der Heiden[1] | Maud van Soest[5]* | Fenny van Egmond[6†]

[1]Cultural Heritage Agency of the Netherlands, Amersfoort, The Netherlands

[2]Groningen Institute of Archaeology (GIA), Groningen, The Netherlands

[3]Department of Chemistry, Metropolitan State University of Denver, Denver, Colorado

[4]Soil Geography and Landscape Group, Netherlands Centre for Luminescence Dating, Wageningen University, Wageningen, The Netherlands

[5]Soil Geography and Landscape Group, Wageningen University, Wageningen, The Netherlands

[6]Medusa Explorations, Groningen, The Netherlands

Correspondence
Hans Huisman, Groningen Institute of Archaeology (GIA), Poststraat 6, 9712ER Groningen, The Netherlands.
Email: h.huisman@cultureelerfgoed.nl

Funding information
Ministry of Education, Culture and Science

Scientific editing by Lisa-Marie Shillito

Abstract

Although visible evidence shows that erosion has damaged many archaeological sites, especially when tilled, there has hitherto been scant attention to its quantitative assessment. Accordingly, the archaeology communities lack insight into whether long-term threats to the stability and integrity of soils at these sites allow these cultural repositories to be preserved for future human generations. Of the techniques that are available to measure erosion rates, few have been tested on the timescales needed. We selected three archaeological sites with high expected erosion rates. We combined optically stimulated luminescence (OSL) dating with analyses of radioactive fallout isotope distributions to assess erosion patterns and rates. An age–depth representation of OSL single-aliquot results was developed to determine past erosion, and to identify stable land surfaces on centennial to millennia timescales. Fall-out isotopes of cesium (Cs) and plutonium (Pu) were suitable for shorter timescales: The $^{240}Pu/^{239}Pu$ ratios and a correlation between activities of $^{239+240}Pu$ and ^{137}Cs demonstrated the weapons testing fallout origin of these isotopes in the ~1952–1966 timeframe. Erosion rates in recent decades ranged from 2 to 6 mm/year on the studied sites. Our results indicate that erosion is not only tied to the past, but keeps on threatening archaeological sites.

KEYWORDS

^{137}Cs, erosion, fallout, OSL, Pu

1 | INTRODUCTION

1.1 | Research outline

The Malta Convention indicates that in situ conservation is the preferred way to protect archaeological sites (Council of Europe, 1992). Dutch legislation makes property or infrastructure developers responsible for in situ preservation of archaeological remains or, if this is not feasible, for excavation (i.e., preservation ex situ; Cultural Heritage Agency, 2016). Unfortunately, archaeological sites can be damaged even if no constructions are planned, by natural or permitted human activities (e.g., plowing). Such processes are also known as "creeping degradation" (van Os & Kosian, 2011). At present, there is no financial safety net to prevent damage by these processes. For many of these processes, too little is known to be able to determine the need and urgency of taking action to prevent further degradation. A key factor is the speed of degradation: H. Huisman and van Os (2016) have proposed that only processes

*Present address: Geography Department, Loughborough University, Epinal Way, Loughborough, Leicestershire LE113TU, UK.

†Present address: ISRIC-World Soil Information and Wageningen Environmental Research, Droevendaalsesteeg 3, 6708PB Wageningen, The Netherlands.

that cause measureable degradation within a generation are relevant in the framework of archaeological heritage management.

Erosion is a well-known problem for archaeological sites, especially where arable farming takes place. Soil without vegetation is sensitive to erosion, while plowing levels off differences in relief and increases erosion intensity (e.g., Behm et al., 2011; Diez-Martín, 2010; Dreibrodt et al., 2013; Govers, Vandaele, Desmet, Poesen, & Bunte, 1994; Poesen et al., 1997; Quine, 1999; Quine et al., 1997; Wilkinson, Tyler, Davidson, & Grieve, 2006). Various tests have been carried out, to characterize rates of this leveling and erosion, both on and outside archaeological sites (Alewell, Meusburger, Juretzko, Mabit, & Ketterer, 2014; An, Zheng, & Wang, 2014; Baartman, Temme, Schoorl, Braakhekke, & Veldkamp, 2012; Gaspar, Navas, Walling, Machín & Gómez-Arozamena, 2013; Olson et al., 2013; Schoorl, Boix Fayos, de Meijer, van der Graaf, & Veldkamp, 2004; Walling, Collins & Sichingabula, 2003; Wilkinson et al., 2006). However, the results are ambiguous, partly because different timescales are used, or because of differences in calculation methods and estimated parameters used (Poreba & Bluszcz, 2008).

To get a better grip on the rate of erosion on archaeological sites due to arable farming, three test locations were selected. These locations have suffered from significant erosion in the recent past, and therefore could be seen as worst-case scenarios. Moreover, relevant data about degradation and conservation was available on these sites as well. Two sites (Beek-Kelmond and Meerssen-Onderste Herkenberg) are located in the Limburg loess landscape, the third (Grote Houw) is an anthropogenic mound (Dutch: *terp* or *wierde*) in the northern coastal landscape. A range of methods and approaches were tested to identify past erosion, and to determine its rates. The results were reported (in Dutch) in three field reports (D. J. Huisman & de Kort, 2017; D. J. Huisman, van der Heiden, et al., 2017; D. J. Huisman, de Groot, de Kort, 2017). Of the methods tested, a comparison of LIDAR measurements from different dates resulted in no unequivocal evidence for erosion in the last 20 years: Reason for this was that within this timeframe the effects of erosion that could be detected in these measurements were smaller than that of (a) biases introduced during data acquisition and (b) plowing-induced changes in surface micro-topography between acquisitions.

In the present publication, we combine the results from the three sites to discuss in more depth the results of two other approaches using optically stimulated luminescence (OSL) dating and anthropogenic fallout tracers to try and determine past and present erosional patterns and rates.

1.2 | Using OSL to derive soil re-distribution and mixing

Over the last two decades, the application of OSL dating has become a cornerstone in earth science and archaeology. Developments are continuing in the method itself as well as in the contexts in which it is applied. Such developments include single-grain dating, statistical methods to recognize and deal with incompletely bleached or mixed samples and the use of feldspar (instead of quartz) to extend the age range. A thorough recent overview, focused specifically on geoarchaeology, is given by Robert et al. (2015). Dating colluvium layers with OSL of quartz sand grains is especially useful to assess to what extent sediment/soil redistribution has occurred (see e.g., Fuchs & Lang, 2009 for an overview on OSL of hillslope deposits). A potential complication is that not all quartz grains are equally exposed to sunlight during plowing and/or soil re-distribution. This heterogeneous bleaching typically results in skewed OSL age distributions where the leading edge typically provides the best age estimate of the last moment of disturbance. Moreover, the soil mixing activities of soil fauna (termed bioturbation) can transport quartz grains deeper into the profile and thus cause mixing of older and younger deposits also contributing to extra scatter in OSL age distributions (e.g., Bateman, Frederick, Jaiswal, & Singhvi, 2003; Reimann, Román-Sánchez, Vanwalleghem, & Wallinga, 2017). Soil mixing and heterogeneous bleaching together, which can co-occur in many colluvial settings, could lead to complex OSL age distributions and thus hampers a straightforward geochronological interpretation of OSL age data.

In contrast, OSL age distributions potentially provide valuable information on earth-surface processes as the nature of within-sample variations manifested in OSL age distributions, especially when recorded on single-grain or close to single-grain level, will depend on the landscape position as well as on erosion/deposition and soil forming processes. We postulate the following patterns for different colluvial circumstances (see Figure 1).

1. In sedimentary environments with little or no soil mixing, the homogenous material is deposited in thin layers. If the material is well-bleached, as for example, in aeolian deposits like loess, the layers are individually well-datable and with little within-sample age scatter. The entire sequence ideally exhibits a sequence that is steadily getting younger with decreasing depth.

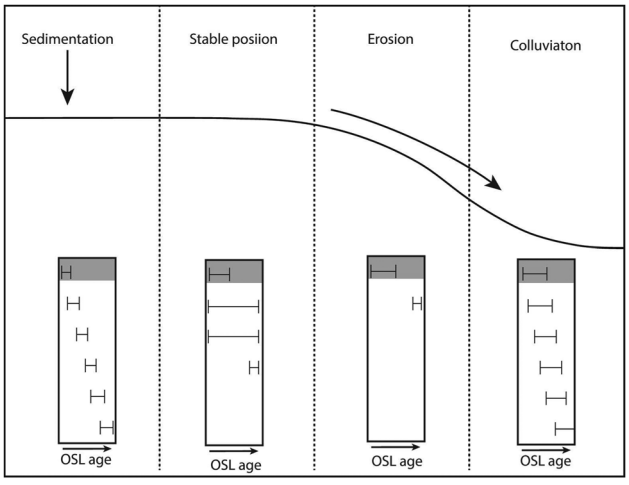

FIGURE 1 Conceptual model of the relation between the distribution of OSL aliquot ages in a sedimentary section or soil profile in different landscape positions. OSL: optically stimulated luminescence

2. In a stable landscape position, the topsoil (A horizon) material—subject to plowing and/or bioturbation which will continuously expose sand grains to sunlight—will be bleached relatively homogenously. The horizon immediately below the topsoil, however (B horizon), will only receive some recently bleached grains by bioturbation as bioturbation rates drop significantly with soil depth (e.g., Reimann et al., 2017). As a result, this layer will contain quartz grains with a wide range of OSL ages, corresponding to the age range of landscape stabilization.
3. On eroding landscape positions, the part of the topsoil (A horizon) that remains after an erosion event will be immediately mixed with older, underlying deposits (B and C horizons) by plowing and bioturbation. As a result, th topsoil will yield a more pronounced scatter of OSL ages, with a truncation of the age–depth profile.
4. At some locations, (slow) sedimentation or colluviation occurs simultaneously with bioturbation. Here, freshly deposited sediment will be mixed with older sediments. Mixing of this material will continue until it is eventually buried, below the active bioturbation zone. This again results in a sequence of steadily younger OSL ages with decreasing soil depth, but with greater spread than in the genuine sedimentary sequence.

A prerequisite for using quartz OSL methods to derive earth-surface processes such as bioturbation, erosion, and deposition is that the analysis is carried out on (quasi) single-grain level to avoid signal averaging of grains with different sediment transport and/or mixing histories (e.g., Arnold & Roberts, 2009). Quartz minerals from the North European plain typically show very low percentages (<5%) of luminescent quartz grains (e.g., Lüthgens, Böse, & Preusser, 2011; Reimann, Lindhorst, Thomson, Murray & Frechen 2012); that is the use of very small aliquots (with ~30 grains) as a proxy for genuine single-grain measurements to disentangle different earth-surface processes is justified (Reimann, Lindhorst, Thomsen, Murray, & Frechen, 2012). In this study, we aim to utilize the variation in very small aliquot OSL age distributions to inform on landscape stability and erosion/sedimentation processes. The rationale behind this is that different earth-surface process regimes are manifested in characteristic OSL age distributions of individual samples as well as OSL age–depth profiles.

1.3 | Weapons testing cesium (^{137}Cs) and plutonium ($^{239+240}$Pu) approaches

Human activities have caused various compounds to accumulate in the environment to levels exceeding the natural background. Of some of these compounds, we can assume that they were more or less evenly distributed in the landscape. Consequently, erosion or other forms of soil displacement result in differences in the concentration of these compounds ("tracers"). Differences in concentrations can, therefore, be used to determine how much material has been moved since the deposition of these compounds. This approach works best if the compounds were introduced into the environment in one or a few single events. This makes specifically the ^{137}Cs and Pu isotopes especially useful—where Pu is measured as the total of an isotope with mass numbers 239 and 240 (hereafter indicated by $^{239+240}$Pu). These isotopes do not occur in nature; in the Netherlands, there are two possible sources for them.

Atmospheric nuclear detonations in the mid-20th century have introduced many synthetic fission products and actinides that accumulate in the environment at detectable levels in most locations of both the northern and southern Hemispheres. From 1952 to 1962, the former Soviet Union and the United States detonated high-yield thermonuclear test weapons that injected radioisotopes into the stratosphere; thereafter, the material returned to the troposphere and was deposited globally. The atmospheric processes resulting in the deposition distributions of "stratospheric fallout" have been extensively discussed (e.g., Bennett, 2002), as have the global geographic distributions of the fallout. The global occurrence of these isotopes allows the application of ^{137}Cs and $^{239+240}$Pu as soil erosion tracers in most locations worldwide. The bomb-test radionuclide tracer approaches have the important features of using isotopes with zero backgrounds that were largely derived from a limited timeframe (1952–1966). However, the 1986 Chernobyl reactor disaster also released large quantities of ^{137}Cs ($t_{1/2}$ = 30 year) that were deposited in vast areas of Eurasia (e.g., Stoutjesdijk, 1986). As a result of the added Chernobyl contributions, the application of ^{137}Cs as a soil erosion tracer in Eurasian field settings entails further challenges in determining a reference inventory, which may be locally much more variable, owing to the tropospheric transport processes that distributed volatile ^{137}Cs. In laboratories applying gamma spectrometry for conventional ^{137}Cs activity measurements, there is no longer the possibility of using short-lived ^{134}Cs ($t_{1/2}$ = 2.7 years) to apportion the total ^{137}Cs inventory between stratospheric fallout and Chernobyl contributions.

In contrast to the broad distribution of volatile ^{137}Cs in Eurasia, actinides such as U, Np, Pu, and Am were released by the failed Chernobyl reactor in the form of non-volatile, micron-size "hot particles" of fuel. These hot particles became distributed in a more limited geographic zone, as discussed elsewhere (e.g., Ketterer, Hafer, & Mietelski, 2004; Mietelski & Was, 1995). Recent work (Alewell et al., 2014; Alewell, Pitois, Meusburger, Ketterer, & Mabit, 2017) has shown $^{239+240}$Pu to be an advantageous, Chernobyl-devoid soil erosion tracer in central Europe. The activities of Pu are commonly expressed as $^{239+240}$Pu, the summed activities of ^{239}Pu ($t_{1/2}$ = 24,110 years) and ^{240}Pu ($t_{1/2}$ = 6,563 years). An additional advantage of $^{239+240}$Pu that renders it attractive, in comparison to ^{137}Cs, is that the long-lived ^{239}Pu and ^{240}Pu isotopes are readily analyzed in large sample sets by inductively coupled plasma mass spectrometry (Ketterer & Szechenyi, 2008; Ketterer, Zheng & Yamada, 2012), a capability present in thousands of labs worldwide. The inductively coupled plasma mass spectrometry (ICP-MS) measurement process, as well as all forms of mass spectrometry, entails separate measurements of ^{239}Pu and ^{240}Pu, permitting the use of the atom ratio ^{240}Pu/^{239}Pu as a provenance tool; one can, therefore, probe whether the tracer itself originates entirely from the assumed ubiquitous stratospheric fallout, and is unaffected by other

local/regional sources of Pu (e.g., Nevada Test Site, Chernobyl, Sellafield, and Rocky Flats).

To apply the tracer approach in a localized study area, one must measure a reference inventory that is assumed to reflect the initial depositional inventory (expressed as Bq/m^2). The measurement of a reliable reference inventory is challenging in many settings and must include multiple inventory measurements within close proximity (10^1–10^3 m) to unknown locations being investigated within the test landscape. The reference inventory is used as an assumed baseline of zero erosion against which, differences in ^{137}Cs or $^{239+240}$Pu inventories are modeled in terms of soil erosion or deposition rates, typically expressed in ton/ha/year (Ritchie & McHenry, 1990). In the present study, however, due to the intense agriculture in the research areas, it is virtually impossible to find a location in the research areas where such stable conditions can reliably be assumed.

Various methods have been used to calculate erosion rates, employing differences in the concentrations of fallout isotope in soil profiles (An et al., 2014, Gaspar, Navas, Walling, Machín, & Gómez Arozamena, 2013; Kachanoski, 1993; Quine, 1999; Quine et al., 1997; Ritchie & McHenry, 1990; Schoorl et al., 2004; Walling & Quine, 1990, 1991, 1992; Wilkinson et al., 2006; Zhang, Higgitt & Walling, 1990; Zhang, Quine, & Walling, 1998). The outcomes of these calculation methods, however, depend to such a degree on assumptions and estimates of key parameters that different methods may produce widely different outcomes (Poreba & Bluszcz, 2008). Moreover, most researchers study natural (non-plowed) soils, where the distribution of tracers in a soil profile can be approached by diffusion models. In our sites, however, the tracer distribution in a profile is dominantly determined by soil cultivation. In general, this implies a homogeneous concentration of tracers in the topsoil whereas the effects of leaching and of bioturbation are assumed negligible. Moreover, these methods usually express erosion in weight of displaced soil per area (e.g. ton·ha^{-1}·year^{-1}). For the present study, however, the severity of erosion is determined by the decrease in ground level, for example, in mm/year. Finally, as mentioned above, finding an undisturbed soil profile with no erosion or sedimentation, and with no human activities that may have affected the concentration of ^{137}Cs and $^{239+240}$Pu is neigh impossible in the research areas. We can assume, however, that field boundaries —which were unchanged during the period of interest—prevent transport of colluvium except in extreme circumstances. With these boundary conditions, we developed a different method for calculating erosion rates.

Assuming negligible leaching or bioturbation, topsoil erosion will result in a decrease in the total amount of tracers in a soil profile, proportionally to the loss of relative topsoil thickness, that is, a decrease of 10% tracer content in a soil profile would correspond to a 10% reduction in topsoil thickness (e.g., 3 cm for a 30-cm topsoil). However, we need to take into account soil cultivation during the period of erosion: If an erosion event resulted in a decrease in the thickness of the topsoil (and if all tracers are in the topsoil), the next round of plowing will incorporate fresh, tracer-free material from deeper in the profile into the plow layer. A next erosion event will remove fewer tracer-components from the profile, as some are now present are greater depth whereas the tracers are diluted with tracer-poor material from greater depths. As a result, a single erosion event of for example, 20% of the plow soil thickness will cause a greater loss of tracers in the soil profile than two 10% erosion events with a plow event in between. This makes the relationship between erosion and the decrease of tracers dependent on the intensity and frequency of erosion events, and of the frequency of plowing. Within these boundaries, erosion rates can be calculated with the formula (see also Figure 2).

$$\frac{\mathrm{Tr}_t}{\mathrm{Tr}_0} = \left(1 - \frac{e}{D}\right)^{n_t} \quad (1)$$

where Tr_0 is the tracer content at start (this is estimated as average in the present study), Tr_t the tracer content after t years of erosion (measured); D the plow depth (mm); t the time (years), n_t the erosion occurrence per year, e the erosion (mm/event), E_t the total erosion (mm) in time t; E the average erosion (mm/year).

Figure 2 shows the ratio of tracer content to average erosion rate for different frequencies of erosion events. Assumptions are that tracer deposition happened 50 years ago in one event, a topsoil thickness of 30 cm and one plow event per year, thoroughly mixing the topsoil. The graph not only shows how the estimated erosion rate depends on the frequency of erosion events, with high-frequency small erosion events causing smaller traces losses than one or a few larger erosion events, even if the total loss of soil material is the same. This makes erosion rate estimates from tracers especially unreliable at high erosion rates, especially at values of Tr_t / Tr_0 < 0.2.

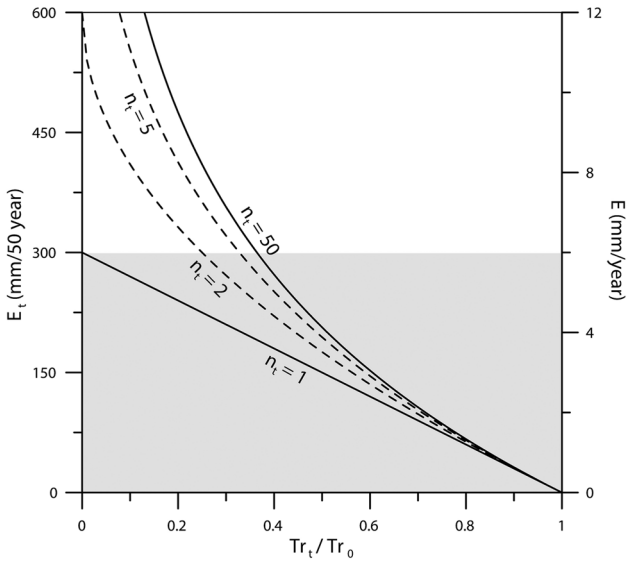

FIGURE 2 Schematic representation of the theoretical relationship between the rates of erosion (E; erosion per year, and E_t; cumulative erosion in 50 years), and the relative change in tracer concentrations ($\mathrm{Tr}_t/\mathrm{Tr}_0$) for different frequencies of erosion events between plowing (n_t, where n_t stands for number of erosion events in 50 years). The gray plane indicates the plow depth (in this calculation 30 cm)

Keeping in mind this limitation, overall erosion rates can be estimated from tracer concentrations by converting erosion per event(s) to the average erosion (mm/year, E). This is possible by inserting formulas $e = (E_t)/n_t$ and $E = E_t/t$ (i.e., $E = E \times t/n_t$):

$$\frac{\mathrm{Tr}_t}{\mathrm{Tr}_0} = \left(1 - \frac{E_t}{Dn_t}\right)^{n_t} \quad (2)$$

If we want to calculate the average erosion rate from the measured tracers we need to convert this formula to:

$$E = \frac{Dn_t\left(1 - \sqrt{\frac{\mathrm{Tr}_t}{\mathrm{Tr}_0}}\right)}{t} \quad (3)$$

2 | TEST LOCATIONS

The *Beek-Kelmond* site lies in the loess area of Zuid-Limburg (Southeast Netherlands), ~1 km south of the village Beek on the southern edge of the Graetheide plateau (See Figure 3). The site is bordered by an asphalt road and a small brook valley. The terrain consists of a plateau that slopes towards the west and southwest. On the east side, a saddle is located (Figure 4a,b). On this site, remains of a settlement from the Early Neolithic Linear Pottery Culture (LBK; 5,300–4,900 BC) include fragments of ceramics and flint as well as soil features that include a moat-like object. It is one of a group of LBK settlement sites in the region; one of the few that has not been damaged by construction work in the last decades, and the only one still remaining in situ that has evidence for a moat-like object (Brounen & Rensink, 2007). Archaeological remains have been recovered from the surface; soil features can be expected to depths of at least 1 m.

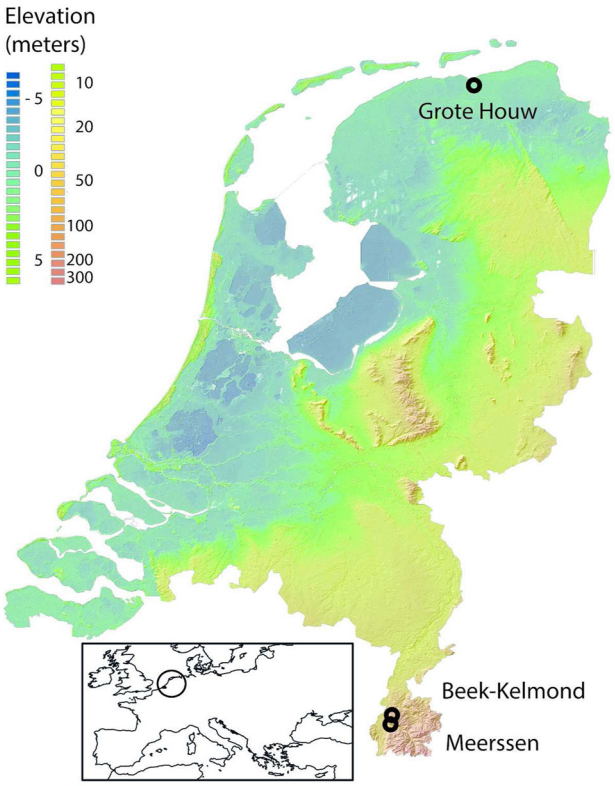

FIGURE 3 Locations of the test sites indicated on the elevation map of The Netherlands [Color figure can be viewed at wileyonlinelibrary.com]

Meerssen Onderste Herkenberg ("Meerssen") is also in the Southeast of the Netherlands, and is the site of a large Roman *villa* (Figure 3). This villa was part of a concentration of villae north of the Geul river between Meerssen and Valkenburg, Most of these *villae*, including Meerssen, lies near a south facing hillside or edge of a plateau overlooking a valley. Meerssen seems to be the largest of the know villae, and among the richest. The site is a listed monument. The Meerssen site is located on the ~1 km long southern slope of the Herkenberg hill which is divided by the N587 road (See Figure 5a,b). The upper part of the hill is quite steep. The lower part forms a relatively flat area with increasingly steep slopes to the south (>8%). Previous archaeological research and geophysical measurements have shown that the main building of the villa lay close to the N587 road, and that additional buildings were present downslope (de Groot, 2005; D. J. Huisman, de Groot, et al., 2017). Archaeological remains are present at the surface. Underneath the plow zone a layer with archaeological finds overlays floors, foundations and robber trenches to a depth of up to several meters.

Grote Houw lies in the North of the Netherlands in the Groningen-Friesland intratidal landscape (see Figure 3). This area was colonized from the iron age onwards while sedimentation and coastal expansion was ongoing. Settlements were situated on artificial mounds that protected them from flood water. Such mounds are locally known as "wierde." Grote Houw is one of a row of settlement mounds on a low ridge (Wehe–Leens–Ulrum–Houwerzijl) that was colonized in the early medieval period; the earliest archaeological finds the date from the Carolingian period (8th–9th century AD). It forms a pair of mounds together with the Kleine Houw (Landschapsbeheer Groningen, 1995) and were used until dike construction in the 11th or 12th century AD stopped flooding of the area. Many other wierde sites have been mined for fertilizer in the 19th and early 20th century. Grote Houw is one of a minority that has escaped this damage. Moreover, its preservation is facilitated because no modern houses are present on it. The study area lies on the eastern part of the Grote Houw, south of the Ulrum-Leens road (Figure 6a,b). The steepest slope (~ 8%) lies on the edge of the eastern part of the mound. The southern part of the plot is remarkably flat. The mound—which consists entirely of anthropogenic deposits—reaches thicknesses of up to 3 m.

3 | MATERIALS AND METHODS

3.1 | Fieldwork

The data from previous archaeological research using trenches (Beek-Kelmond and Meerssen) were combined with data from hand augering (not shown) to select sample locations. These lay basically on the top, halfway along the slope and at the toe of the

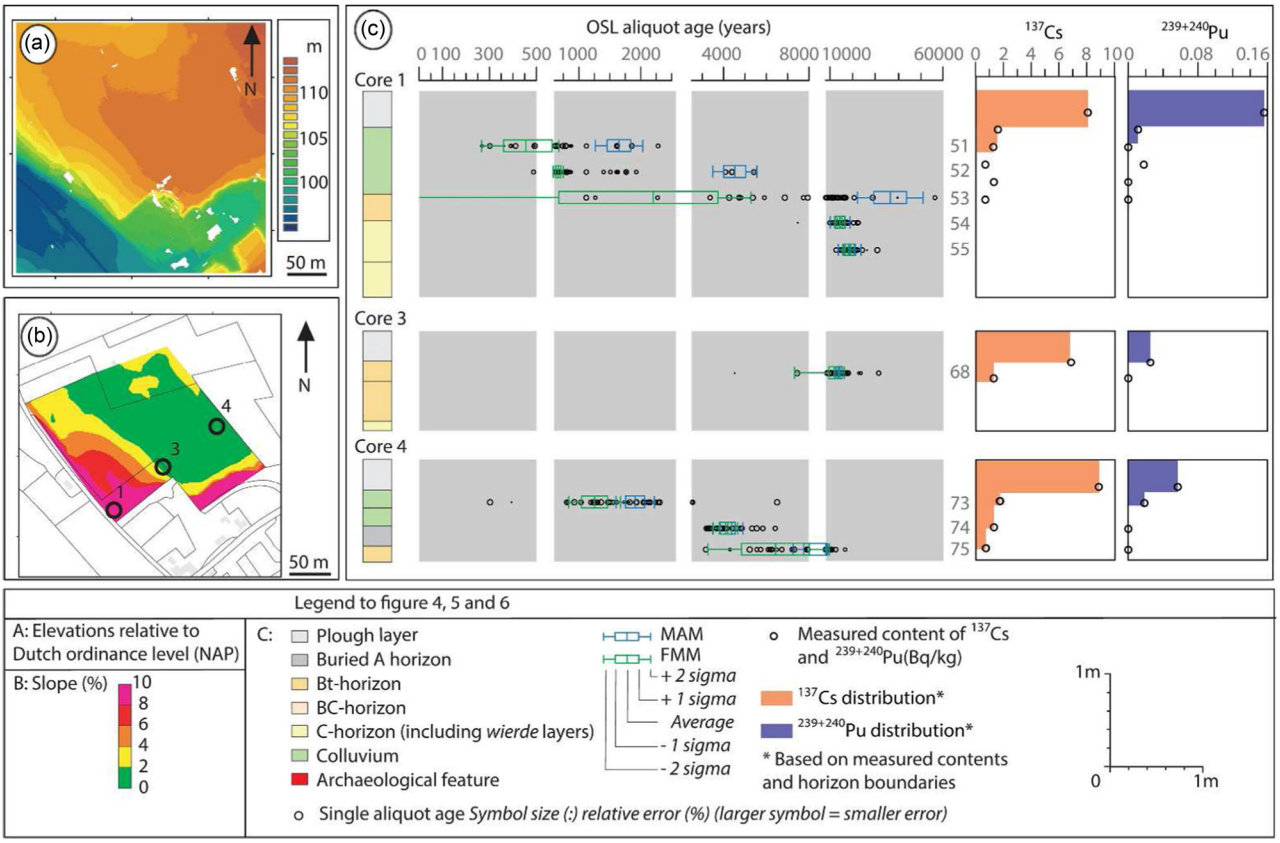

FIGURE 4 Beek-Kelmond site data and measurement results. (a) Elevation map. (b) Slope classes. (c) Depth plots with OSL data (left) and fallout isotope measurements (right). For the OSL single-aliquot SAR–OSL ages—where larger symbols represent smaller errors—are combined with and bsMAM and FMM_{oldest}. Note that the time axis is divided for better readability. bsMAM and FMM_{oldest} symbols are cut off at year 0. In the fallout isotope plots, circles indicate the sample depth and measured concentrations. Colored bars indicate the concentration profile with depth used for the erosion rate calculation. These were based on measured concentrations and the horizon boundaries—assuming that the horizons are homogeneous—but restricted to the upper deposits and neglecting the deeper samples). bsMAM: bootstrapped Minimum Age Model; FMM_{oldest}: oldest component of the Finite Mixture Model; OSL: optically stimulated luminescence; SAR: single-aliquot regenerative [Color figure can be viewed at wileyonlinelibrary.com]

slope. On Beek-Kelmond and Meerssen, mechanical corings produced 10 cm wide undisturbed sediment cores that were used for profile description and sampling (see below). At the Grote Houw, five sample locations were chosen to better represent the more complex elevation map of the site. Here, test pits were dug on each sample location until the depth of undisturbed archaeological layers—usually ~50 cm deep. Samples here were taken directly from the profile.

The mechanical cores were cut in half in a dedicated dark room with subdued red/orange light illumination at TNO/Deltares to prevent the OSL signal from being affected by light exposure. One half of the core was used under daylight condition to make a full lithological/pedological description of the core and to determine OSL sample depths. The OSL samples were taken in the dark room from the remaining half-core, which was not daylight exposed. To prevent contamination sediment too close to the casing (<1 cm) was discarded from OSL sampling. The OSL samples were wrapped in double sealed thick black plastic to prevent exposure to light. In the profile pits of Grote Houw, OSL samples were taken by hammering ~5 cm wide PVC tubes into the profile. The tubes were subsequently dug out, closed at both ends and packaged. The samples were then shipped to the Dutch Centre for Luminescence Diagnostics (NCL) in Wageningen for OSL analysis.

Samples for the ^{137}Cs and $^{239+240}Pu$ tracers were taken as much as possible on the same depths as the OSL samples, but also the complete topsoil was sampled. The ^{137}Cs samples were collected in specially designed round plastic (300 ml) sample boxes and were sent to the lab of Medusa company for analysis. The $^{239+240}Pu$ samples of about 5–10 g were taken in plastic sample bags and processed for $^{239+240}Pu$ analytical work.

3.2 | OSL analyses

The OSL samples were split into two subsamples: One subsample was prepared for the palaeodose, one was used for dose rate determination. For the sample tubes from Grote Houw the sediment at the ends of the PVC tube—material that may have been exposed to light—was taken for the dose rate measurements.

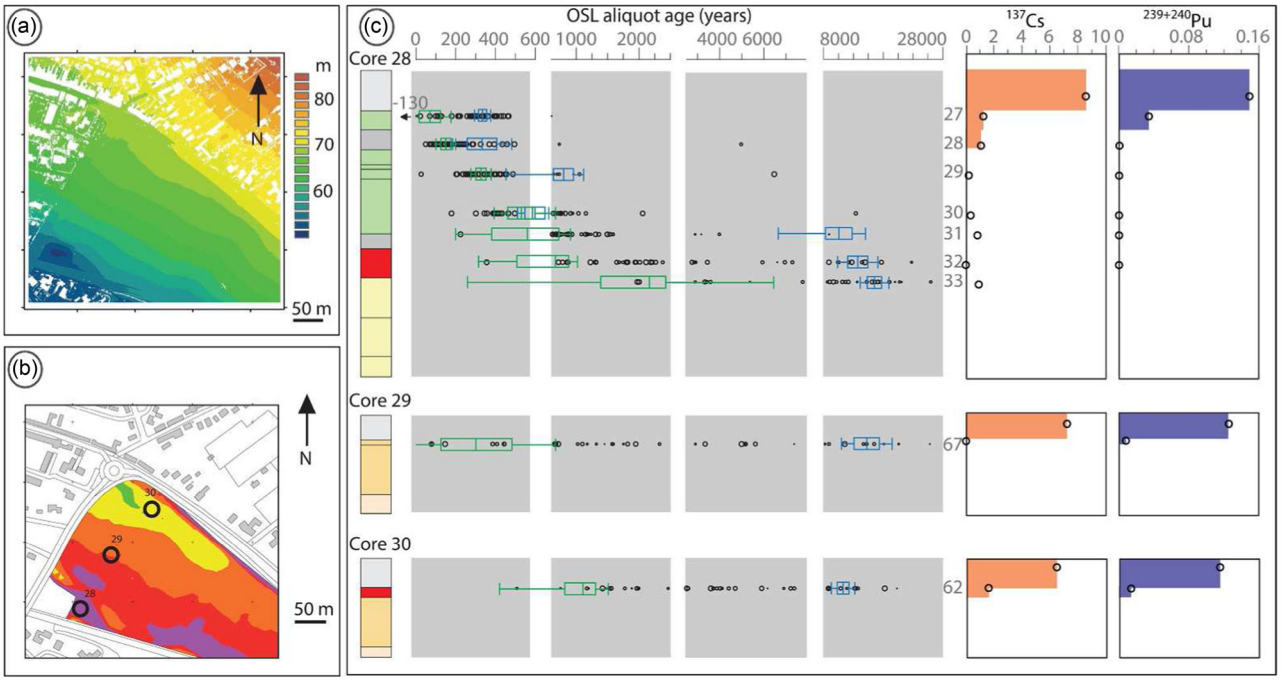

FIGURE 5 Meerssen-Herkenberg site data and measurement results (see Figure 4 for legend and descriptive caption). OSL: optically stimulated luminescence [Color figure can be viewed at wileyonlinelibrary.com]

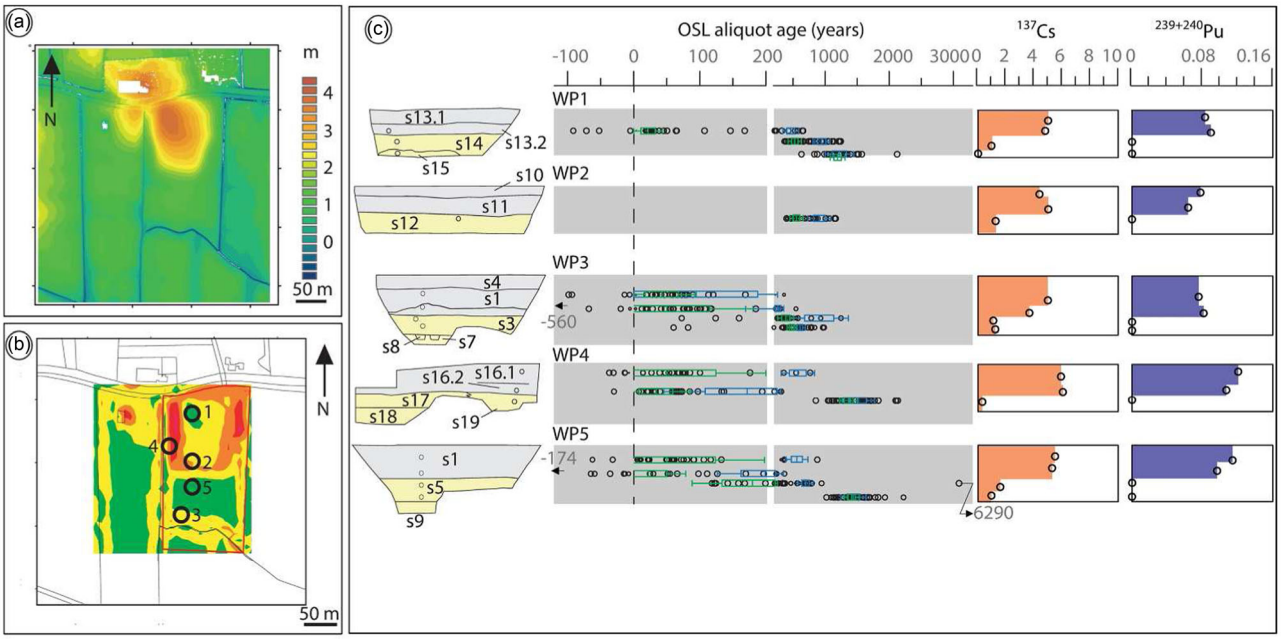

FIGURE 6 Grote Houw site data and measurement results (see Figure 4 for legend and descriptive caption). OSL: optically stimulated luminescence [Color figure can be viewed at wileyonlinelibrary.com]

The palaeodose subsample was wetly sieved to obtain uniform grain-size fractions. For Meerssen the 212–250 μm was used. For Grote Houw the 125–180 μm fraction and for Beek-Kelmond the 90–180 μm was used. These fractions were treated with HCl and H_2O_2 to remove carbonates and organic matter, respectively. The quartz was separated from other minerals using density separation and subsequently treated with hydrofluoric acid to remove the α-irradiated outer rim of the grains and remaining feldspar contaminations. Thereafter, the fraction was wetly sieved again to obtain a purified quartz fraction.

To determine the palaeodose we carried out dose equivalent (D_e) measurements on Risø TL/OSL-DA-20 and Risø TL/OSL-DA-15

readers by applying the single-aliquot regenerative (SAR) dose protocol suggested by Murray and Wintle (2003) on very small aliquots. Each aliquot consisted of a sample disc containing ~14, ~29, and ~38 grains on a 1-mm diameter sample for Meerssen, Grote Houw, and Beek-Kelmond, respectively. At least 48 aliquots (typically ~72) per sample were measured to obtain a batch of at least 20 suitable single-aliquot D_e results after applying standard rejection criteria. The most light-sensitive OSL signal of quartz grains was selected using the "Early Background' approach (Cunningham & Wallinga, 2010). To adjust the measurement conditions we carried out combined preheat plateau/dose recovery as well as thermal transfer experiments on representative samples for each location. Eventually, a preheat/cut heat combination of 200/180°C was selected for all samples. To test the performance of this set-up additional dose recovery experiment on every sample were performed. For samples from location Grote-Houw the average dose recovery ratio was 1.03 ± 0.01 (n = 36). For the location, Meerssen and Beek-Kelmond the dose recovery ratios were calculated to 0.98 ± 0.01 (n = 60) and 0.99 ± 0.01 (n = 36), respectively. Thus, dose recovery experiments confirm the suitability of our samples for OSL dating as well as the robustness of the D_e measurement approach.

To determine sample palaeodoses, and eventually age estimates, two age models were applied to the typically very broad and scattered D_e distributions. To calculate the first palaeodose the bootstrapped Minimum Age Model (bsMAM) of Cunningham and Wallinga (2010) was used. This first palaeodose estimates the amount of charge that was accumulated since the sample left the soil reworking zone and thus is interpreted as the age of the last disturbance or the stabilization age. Based on a pre-analysis of the minimum over-dispersion (i.e. over-dispersion in a well-bleached unmixed sample) observed in the D_e distributions of the three data sets the sigma_b input parameter was set to 20 ± 5% for samples from Meerssen and Beek-Kelmond; for samples Grote Houw this parameter was set to 16 ± 3%. To determine the second palaeodose that corresponds to the initial disturbance of the sample by geological deposition or initial soil erosion and redistribution the oldest component of the Finite Mixture Model (FMM_{oldest}) was utilized. More details of the finite mixture model can be found in Arnold and Roberts (2009) and Reimann et al. (2012). D_e components including <5% of the D_e estimates were discarded to be less depending on single outliers. The same sigma_b values as for the bsMAM were used as model input.

For the dose rate measurement, subsamples were dried overnight at 105°C to determine the in situ water content. The measured water content values are typically around 20% and show only minor variations. Subsequently, the subsamples were placed in the ashing oven (500°C) to remove organic matter and to determine its content. The water and organic matter content were added for each sample to obtain the soft-component attenuation factor (Madsen, Murray, Andersen, Pejrup, & Breuning-Madsen, 2005). The dry dose rates (see below) were corrected for this soft-component attenuation using the procedure outlined in Aitken (1985). The ashed sediment was ground before making 2 × 9 or 1 × 9 cm pucks of a mixture of 70% sediment and wax. Using a Canberra broad energy HPGe gamma spectrometer (Mirion Technologies (Canberra), Inc. Meriden, CT), the activity of series of isotopes within the U and Th decay chain and of ^{40}K was measured and converted into dose rate using the conversion factors described in Guérin, Mercier, and Adamiec (2011). The cosmic dose rate was thereafter calculated based on the geographic location of the sampling site (Prescott & Hutton, 1994) and information on the burial history. All environmental dose rate data are listed in Table 1.

3.3 | Isotope analyses

^{137}Cs analysis was done with a MEDUSA NaI γ-ray detector (MEDUSA Exploration BV, Groningen, The Netherlands), after which the total activity of the nuclides was determined with a full spectrum analysis, following NVN 5695, now incorporated in the Dutch norm for radioactivity measurements (NVN 5666; NEN, 2009). Dry mass of the samples was determined after heating to 130°C. The number of counts specific for ^{137}Cs spectrum was extracted and divided by the dry mass of the sample.

Soil aliquots of ~5–10 g were used for $^{239+240}$Pu analyses, which were conducted after dry-ashing of the soil at 600°C to remove organic matter. Samples were leached with HNO_3 in the presence of a ^{242}Pu yield tracer; the chemical separations and mass spectrometry were conducted using procedures described in Ketterer, Hafer, Jones, and Appleby (2004) and Ketterer and Szechenyi (2008). The validity of the $^{239+240}$Pu activity results was confirmed through analyses of control soils of known activity; the analysis of negative controls (soils and rocks devoid of $^{239+240}$Pu activity) established detection limits of ≤0.01 Bq/kg $^{239+240}$Pu.

The Pu fractions prepared from the samples were analyzed using a Thermo X Series II quadrupole ICP-MS (Thermo Fisher Scientific, Bremen, Germany) located at the Northern Arizona University; a high-efficiency de-solvating sample introduction system (APEX HF; ESI Scientific, Omaha) was used to enhance sensitivity for the low concentrations of ^{239}Pu and ^{240}Pu encountered for soil extracts. Mass spectrometric signals were collected for ^{238}U, ^{239}Pu, ^{240}Pu, and ^{242}Pu in a peak-jumping routine with dwell times of 10 ms; mass discrimination and $^{238}U^{1}H^{+}$ interference corrections upon $^{239}Pu^{+}$ were developed using measurements of a 0.5 µg/l naturally occurring U solution (^{238}U/^{235}U atom ratio = 137.88) as discussed elsewhere (Ketterer et al., 2004).

4 | RESULTS

4.1 | OSL age results

The results of the OSL SAR analyses are presented in age–depth plots for each site in Figures 4c, 5c, and 6c. For readability, the time axis is broken into several linear sections. We furthermore plot the bsMAM age (stabilization age) and with the FMM_{oldest} age the age of the initial disturbance (see Section 3.2) with their 1- and 2-sigma errors—the data are also given in Table 2.

TABLE 1 Optically stimulated luminescence (OSL) dose rate table

Core or profiles	Sample_ID OSL	Depth (m)	Field code	Grain size range (μm)	(% per mass)		Radionuclide concentrations (Bq/kg)			Internal dose rate (Gy/ka)	External dose rate (Gy/ka)		Cosmic dose rate (Gy/ka)	Total dose rate (Gy/ka)
					Water content	Organic content	U	Th	K-40	α	β	γ		
Grote Houw														
1	NCL-9214098	0.25	1,042	125–180	20 ± 5	2.8 ± 0.3	29.6 ± 0.4	29.3 ± 0.8	479 ± 10	0.01 ± 0.005	1.26 ± 0.05	0.74 ± 0.03	0.27 ± 0.01	2.28 ± 0.06
	NCL-9214099	0.35	1,043	125–180	22 ± 6	3 ± 0.3	28.4 ± 0.4	32.4 ± 0.9	514 ± 10	0.01 ± 0.005	1.27 ± 0.05	0.76 ± 0.04	0.26 ± 0.01	2.31 ± 0.07
	NCL-9214100	0.45	1,044	90–125	22 ± 6	2.2 ± 0.2	27.5 ± 0.3	31.7 ± 0.8	501 ± 10	0.01 ± 0.005	1.31 ± 0.05	0.8 ± 0.04	0.25 ± 0.01	2.37 ± 0.07
2	NCL-9214101	0.35	1,034	90–125	20 ± 5	2.3 ± 0.2	30.1 ± 0.4	32.7 ± 0.9	525 ± 10	0.01 ± 0.005	1.38 ± 0.06	0.81 ± 0.04	0.26 ± 0.01	2.46 ± 0.07
3	NCL-9214102	0.2	1,008	125–180	18 ± 4	2.5 ± 0.3	29.8 ± 0.4	29.7 ± 0.8	475 ± 10	0.01 ± 0.005	1.3 ± 0.05	0.76 ± 0.04	0.27 ± 0.01	2.34 ± 0.07
	NCL-9214103	0.35	1,009	125–180	17 ± 4	2.2 ± 0.2	29.9 ± 0.4	28.3 ± 0.8	463 ± 9	0.01 ± 0.005	1.27 ± 0.05	0.77 ± 0.04	0.26 ± 0.01	2.31 ± 0.06
	NCL-9214104	0.45	1,010	125–180	17 ± 4	1.6 ± 0.2	27.4 ± 0.4	29.8 ± 0.8	477 ± 10	0.01 ± 0.005	1.3 ± 0.05	0.81 ± 0.04	0.25 ± 0.01	2.37 ± 0.07
	NCL-9214105	0.55	1,011	125–180	18 ± 4	1.5 ± 0.2	28.8 ± 0.4	29.7 ± 0.9	478 ± 10	0.01 ± 0.005	1.3 ± 0.05	0.8 ± 0.04	0.25 ± 0.01	2.35 ± 0.07
4	NCL-9214106	0.1	1,055	125–180	20 ± 5	2.6 ± 0.3	30.3 ± 0.4	28.9 ± 0.8	470 ± 10	0.01 ± 0.005	1.26 ± 0.05	0.64 ± 0.03	0.28 ± 0.01	2.19 ± 0.06
	NCL-9214107	0.3	1056	125–180	18 ± 5	2.8 ± 0.3	29.6 ± 0.4	27.1 ± 0.8	460 ± 9	0.01 ± 0.005	1.25 ± 0.05	0.76 ± 0.04	0.26 ± 0.01	2.29 ± 0.06
	NCL-9214108	0.4	1,057	125–180	18 ± 5	1.4 ± 0.1	27.5 ± 0.3	27.9 ± 0.8	460 ± 9	0.01 ± 0.005	1.23 ± 0.05	0.75 ± 0.03	0.26 ± 0.01	2.25 ± 0.06
5	NCL-9214109	0.15	1,021	125–180	18 ± 4	2.2 ± 0.2	29.6 ± 0.3	27.3 ± 0.6	459 ± 8	0.01 ± 0.005	1.26 ± 0.05	0.69 ± 0.03	0.28 ± 0.01	2.23 ± 0.06
	NCL-9214110	0.3	1,022	125–180	20 ± 5	1.9 ± 0.2	28.7 ± 0.4	28 ± 0.8	468 ± 10	0.01 ± 0.005	1.24 ± 0.05	0.74 ± 0.03	0.26 ± 0.01	2.25 ± 0.06
	NCL-9214111	0.4	1,023	125–180	18 ± 5	1.5 ± 0.2	26.9 ± 0.3	26.8 ± 0.8	467 ± 10	0.01 ± 0.005	1.24 ± 0.05	0.75 ± 0.03	0.26 ± 0.01	2.26 ± 0.06
	NCL-9214112	0.55	1,024	125–180	21 ± 5	1.8 ± 0.2	27.2 ± 0.3	29.4 ± 0.8	481 ± 10	0.01 ± 0.005	1.25 ± 0.05	0.78 ± 0.04	0.25 ± 0.01	2.29 ± 0.06
Meerssen														
28	NCL-9314113	0.4	27	212–250	21 ± 5	2.1 ± 0.2	52 ± 0.6	48.6 ± 1.2	626 ± 12	0.01 ± 0.005	1.75 ± 0.12	1.22 ± 0.06	0.25 ± 0.01	3.24 ± 0.13
	NCL-9314114	0.7	28	212–250	24 ± 6	2.9 ± 0.3	53.3 ± 0.5	49.4 ± 1	630 ± 12	0.01 ± 0.005	1.72 ± 0.12	1.23 ± 0.07	0.24 ± 0.01	3.19 ± 0.14
	NCL-9314115	1	29	212–250	25 ± 6	1.9 ± 0.2	50.1 ± 0.5	48.7 ± 1.1	611 ± 12	0.01 ± 0.005	1.67 ± 0.13	1.22 ± 0.07	0.22 ± 0.01	3.12 ± 0.14
	NCL-9314116	1.4	30	212–250	25 ± 6	1.9 ± 0.2	42.7 ± 0.5	41 ± 1	518 ± 10	0.01 ± 0.005	1.38 ± 0.1	0.97 ± 0.06	0.21 ± 0.01	2.57 ± 0.12
	NCL-9314117	1.6	31	212–250	22 ± 6	1.5 ± 0.1	51 ± 0.5	46.3 ± 1.1	634 ± 12	0.01 ± 0.005	1.75 ± 0.12	1.23 ± 0.07	0.21 ± 0.01	3.19 ± 0.14
	NCL-9314118	1.9	32	212–250	21 ± 5	1.2 ± 0.1	43.6 ± 0.5	41.4 ± 1	541 ± 11	0.01 ± 0.005	1.51 ± 0.1	1.06 ± 0.06	0.2 ± 0.01	2.77 ± 0.12
	NCL-9314119	2.1	33	212–250	22 ± 5	1 ± 0.1	46.4 ± 0.5	44.1 ± 1	536 ± 11	0.01 ± 0.005	1.49 ± 0.1	1.05 ± 0.06	0.2 ± 0.01	2.74 ± 0.12
29	NCL-9314120	0.23	67	212–250	20 ± 5	2.3 ± 0.2	44.1 ± 0.5	42.7 ± 1	539 ± 11	0.01 ± 0.005	1.47 ± 0.1	0.96 ± 0.05	0.27 ± 0.01	2.7 ± 0.11
30	NCL-9314121	0.24	62	212–250	20 ± 5	1.8 ± 0.2	52.6 ± 0.5	50.5 ± 1	686 ± 13	0.01 ± 0.005	1.89 ± 0.12	1.26 ± 0.06	0.26 ± 0.01	3.42 ± 0.14
Beek-Kelmond														
1	NCL-9414122	0.55	51	90–180	19 ± 5	1.6 ± 0.2	41.7 ± 0.5	41.3 ± 1	529 ± 11	0.01 ± 0.005	1.55 ± 0.1	1.03 ± 0.05	0.25 ± 0.01	2.83 ± 0.12
	NCL-9414123	0.8	52	90–180	18 ± 4	1.6 ± 0.2	43.2 ± 0.5	43.2 ± 1	528 ± 11	0.01 ± 0.005	1.57 ± 0.1	1.05 ± 0.05	0.23 ± 0.01	2.86 ± 0.11
	NCL-9414124	1.05	53	90–180	21 ± 5	2.3 ± 0.2	46.9 ± 0.4	47.3 ± 0.8	584 ± 11	0.01 ± 0.005	1.66 ± 0.11	1.1 ± 0.06	0.22 ± 0.01	2.99 ± 0.13
	NCL-9414125	1.3	54	90–180	18 ± 5	1.1 ± 0.1	45.7 ± 0.5	46 ± 1.1	554 ± 11	0.01 ± 0.005	1.65 ± 0.11	1.1 ± 0.06	0.21 ± 0.01	2.97 ± 0.12
	NCL-9414126	1.55	55	90–180	13 ± 3	1.8 ± 0.2	43 ± 0.5	43.2 ± 1	536 ± 11	0.01 ± 0.005	1.65 ± 0.09	1.07 ± 0.05	0.25 ± 0.01	2.98 ± 0.11
3	NCL-9414127	0.45	68	90–180	22 ± 5	1.9 ± 0.2	45.4 ± 0.5	44.3 ± 1.1	572 ± 11	0.01 ± 0.005	1.61 ± 0.11	1.04 ± 0.06	0.25 ± 0.01	2.91 ± 0.13
4	NCL-9414128	0.45	73	90–180	22 ± 5	1.8 ± 0.2	41.8 ± 0.5	41.1 ± 1	556 ± 11	0.01 ± 0.005	1.54 ± 0.11	0.99 ± 0.05	0.25 ± 0.01	2.8 ± 0.12
	NCL-9414129	0.7	74	90–180	23 ± 6	1.8 ± 0.2	49.1 ± 0.6	46.2 ± 1.2	669 ± 13	0.01 ± 0.005	1.85 ± 0.13	1.21 ± 0.07	0.24 ± 0.01	3.31 ± 0.15
	NCL-9414130	0.9	75	90–180	21 ± 5	1.4 ± 0.1	40.4 ± 0.5	38.8 ± 1	597 ± 12	0.01 ± 0.005	1.61 ± 0.11	1.01 ± 0.05	0.23 ± 0.01	2.87 ± 0.13

TABLE 2 Optically stimulated luminescence (OSL) samples with bootstrapped Minimum Age Model (bsMAM) and the oldest component of the Finite Mixture Model (FMM_{oldest}) ages

Sites	Core or profile	Sample_ID OSL	Depth (m)	MAM age (ka)	Error MAM age (ka)	FMM_{oldest} age (ka)	Error FMM_{oldest} age (ka)
Grote Houw	1	NCL-9214098	0.25	0.02	0.01	0.48	0.06
		NCL-9214099	0.35	0.57	0.05	0.94	0.06
		NCL-9214100	0.45	1.19	0.06	1.23	0.11
	2	NCL-9214101	0.35	0.56	0.06	0.93	0.08
	3	NCL-9214102	0.2	0.04	0.03	0.09	0.09
		NCL-9214103	0.35	0.05	0.07	0.27	0.05
		NCL-9214104	0.45	0.37	0.04	0.92	0.22
		NCL-9214105	0.55	0.50	0.04	0.64	0.03
	4	NCL-9214106	0.1	0.05	0.08	0.60	0.13
		NCL-9214107	0.3	0.03	0.03	0.18	0.07
		NCL-9214108	0.4	1.36	0.07	1.53	0.13
	5	NCL-9214109	0.15	0.05	0.07	0.58	0.08
		NCL-9214110	0.3	0.02	0.03	0.25	0.06
		NCL-9214111	0.4	0.18	0.04	0.71	0.06
		NCL-9214112	0.55	1.43	0.06	1.44	0.10
Meerssen	28	NCL-9314113	0.4	0.07	0.05	0.33	0.02
		NCL-9314114	0.7	0.15	0.02	0.33	0.07
		NCL-9314115	1	0.33	0.03	0.80	0.18
		NCL-9314116	1.4	0.53	0.07	0.58	0.04
		NCL-9314117	1.6	0.56	0.18	10.9	2.1
		NCL-9314118	1.9	0.69	0.19	13.9	1.7
		NCL-9314119	2.1	3.32	1.53	16.5	1.2
	29	NCL-9314120	0.23	0.31	0.17	15.6	2.0
	30	NCL-9314121	0.24	1.21	0.40	11.4	1.1
Beek-Kelmond	1	NCL-9414122	0.55	0.45	0.10	1.66	0.19
		NCL-9414123	0.8	0.67	0.05	4.55	0.51
		NCL-9414124	1.05	2.18	1.52	37.9	6.5
		NCL-9414125	1.3	14.2	1.1	14.6	2.3
		NCL-9414126	1.55	18.3	1.3	18.8	2.5
	3	NCL-9414127	0.45	11.9	2.3	14.5	0.8
	4	NCL-9414128	0.45	1.26	0.21	1.92	0.15
		NCL-9414129	0.7	4.10	0.29	4.19	0.36
		NCL-9414130	0.9	6.47	1.62	8.22	0.48

In Beek-Kelmond (Figure 4c), the core that lies at the toe of the slope (core 1) show a remarkable succession of single-aliquot age ranges: The sequence starts with two samples (samples 54, 55) that show little spread, centering around Late Pleistocene ages (a single age population with bsMAM = FMM_{oldest})– the period of loess deposition. The sample above (53) also centers around the same period, but in addition, shows single aliquots of older and younger ages resulting in diverging bsMAM and FMM_{oldest} age estimates—ranging from 60,000 to 1,000 years ago. The following two samples (52, 51) have FMM_{oldest} ages in the Neolithic (initial disturbance) and bsMAM ages that indicate iron age to sub-recent stabilization of the soil layers. At the top of the slope (core 4), the sequence of the sample (75–73) compares well with the top three samples (53–51) in core 1, also showing Late Pleistocene to Neolithic ages in the lowest sample, moving to more recent ages at shallower depths. The sample halfway the slope (core 3, sample 68), however, shows a single age population indicating Late Pleistocene to Early Holocene deposition.

In Meerssen (Figure 5c; core 28, the two lower samples (32/18 and 33/19) show a similar spread in dates as the Beek-Kelmond sample 53, indicating initial deposition (FMM_{oldest}) at the Late Pleistocene and a stabilization of the soil layer in Medieval times. In this core, samples are lacking that show an undisturbed depositional age of the initial loess deposition (as in Beek-Kelmond 54 and 55). Apparently, layers of that age are buried deeper. The rest of the sequence (sample 31–27) shows a gradual decrease in age from Medieval to sub-recent, but also a large spread in ages. On the plateau at the top of the slope, and halfway the slope, (cores 29 and 30) the samples—which originate from directly underneath the current plow horizon—both show a large difference between medieval to sub-recent bsMAM and late Pleistocene to early Holocene FMM_{oldest} ages.

The Grote Houw profiles (Figure 6c) show predominately FMM_{oldest} ages corresponding to Medieval times, and some samples indicate recent stabilization of the soil layers through their sub-recent bsMAM ages. The plow layer itself (samples ..98, ..102, ..103, ..106, ..107, ..109, and ..110 in Table 2) show aliquot ages that range from medieval to modern.

4.2 | OSL age interpretation

Although some samples give a large range in different single-aliquot ages, at least some of them may result from signal averaging of

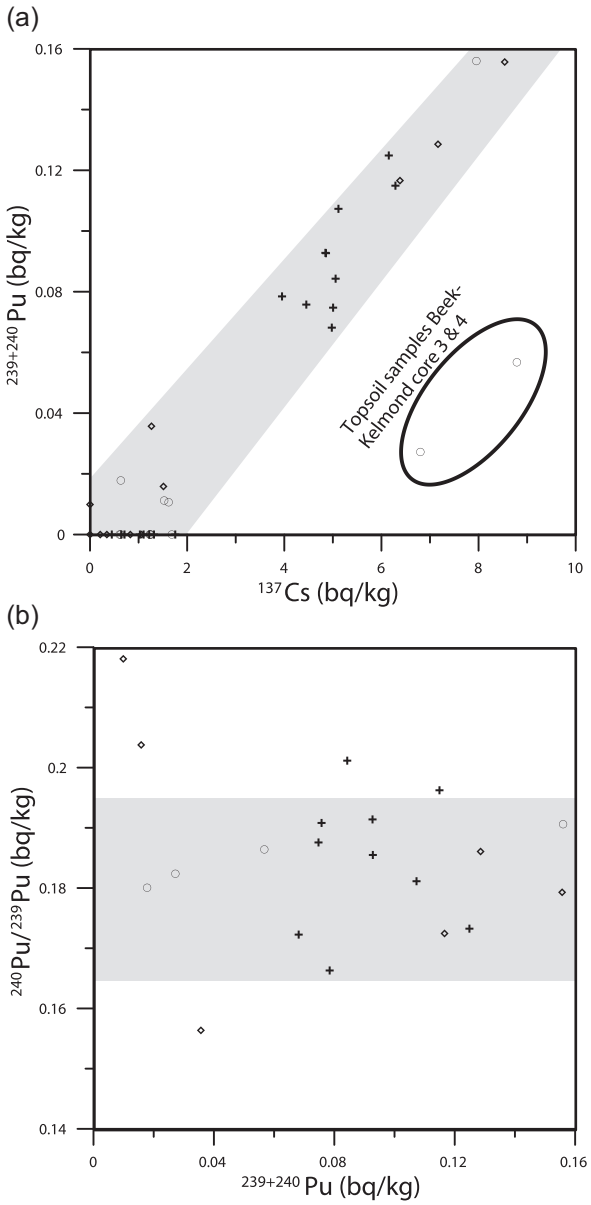

FIGURE 7 General results of 137Cs vs. 239 + 240Pu. (a) Scatterplot showing correlation between Cs and Pu isotopes. Beek Kelmond samples are indicated by circles, Meerssen samples by diamonds and Grote Houw samples by crosses. Two Beek-Kelmond topsoil samples (from core 3 and 4; indicated) fall outside this correlation. (b) 239 + 240Pu concentration versus Pu isotope ratio, showing that at higher concentrations - and therefore higher accuracy and precision - the isotope ratio fall in the range of 0.165–0.195

several grains within one single aliquot. We argue, however, that the differences between FMM_{oldest} and bsMAM and thus the oldest and the youngest age component give an indication of past erosion and colluviation process:

For the loess sites (Beek-Kelmond and Meerssen), the lower sequence in Beek core 1 gives a background in FMM_{oldest} ages corresponding to initial loess deposition. The samples that show a large difference between FMM_{oldest} and bsMAM, from Late Pleistocene to medieval or even sub-recent (Beek 1: 53, Meerssen 28: 31,32,33; 29:67; 30:62) probably represent B or AB horizons that were at stable landscape positions for a long time. Bioturbation at low to moderate rates would have caused transport of bleached grains to these horizons and a bsMAM age that is significantly younger than the age of the initial deposition. Lack of recent dates in core 3 in Beek-Kelmond indicates that this slope position has been subject to erosion, as old single-aliquot ages are found immediately underneath the plow layer (Figure 4c). In contrast, sub-recent single-aliquot ages for core 29 suggest that the slope position at Meerssen site has not been subject to significant erosion (Figure 5c).

The Grote Houw results are in line with the history of anthropogenic mound building on regularly flooded areas, as such they do not add much information with regard to soil redistribution patterns. Most remarkable, however, is that the plow layers of intensively cultivated soils still show FMM_{oldest} ages up to approximately 600 years. Apparently, even intensive plowing is no guarantee for complete mixing of grains. Despite the incomplete mixing, the bsMAM is sufficiently suitable to establish the expected unfinished sample stabilization (Figure 6c), supporting the robustness of all non-modern stabilization ages.

The calculation methods used in this study could have had introduced uncertainties that need to be addressed to ensure proper validity evaluation of the OSL dating results. A potential uncertainty is introduced by calculating the age of initial disturbance from a single sample D_e distribution using the FMM_{oldest}. Ongoing sediment accumulation from the Late Pleistocene to Medieval times and associated changes in environmental conditions (including water content, organic matter, and dosimetry) could have in theory introduce a systematic error to the age of initial disturbance.

However, the spatial variation in the environmental dose rate data (Table 1) is generally small (especially for Beek-Kelmond and Grote Houw) implying that the temporal variation of those parameters is small as well. Moreover, the soils in our locations are not accumulating over time. Rather, typical soil processes have overprinted a genuine geological deposit, the latter being either aeolian, marine, or colluvial of nature. The FMM_{oldest} ages are estimates of the burial time related to the original geological deposition while the stabilization ages (bsMAM) determine the time since the last disturbance; that is the latter are most likely linked to the overprinting soil processes (e.g. bioturbation or plowing). For an undisturbed geological deposit (i.e. not overprinted by soil processes) the initial disturbance age should be equal to the stabilization age. This is nicely illustrated by samples from Meerssen core 1 at depth 1.3 and 1.55 m (Late Pleistocene) and Grote Houw core 5 at a depth of 0.55 m (Late Holocene), providing a first validation of our OSL age interpretation. Furthermore, in all three settings it is unlikely that overprinting by soil processes have changed the lithological configuration and thus the natural background radionuclide composition of our samples. Overprinting soil processes may have had an impact on the samples organic matter and/or water content, however, all measured water content values and the vast majority of organic matter contents overlap within

TABLE 3 Concentrations and calculation of erosion rates from cesium (^{137}Cs) and plutonium ($^{239+240}$Pu)

Sites	Boring or pit nr.	Sample nr.	Sample depth (m)	Feature nr. (Grote Houw)	^{137}Cs (Bq/kg) (*SD*)	Thickness of feature or horizon (cm)	^{137}Cs total in feature or horizon (Bq)	^{137}Cs total in profile or core (Bq)	Average site (Bq)	^{137}Cs; ratio profile/site average	Erosion rate (mm/50 years, n_t = 1)	Erosion rate (mm/50 year, n_t = 50)	Yearly erosion (mm/year)
Grote Houw	3	1,013	0.22	1 + 4	5.01 (0.39)	31	0.103 (0.008)	0.151 (0.013)	0.1303	1.16 (0.10)	No erosion		
Grote Houw	3	1,014	0.4	2	3.95 (0.08)	12	0.032 (0.001)						
Grote Houw	3	1,015	0.5	3	1.03 (0.33)	20	0.016 (0.005)						
Grote Houw	3	1,016	0.59	3	1.32 (0.35)	20							
Grote Houw	5	1,026	0.12	1	5.12 (0.29)	35	0.116 (0.008)	0.145 (0.014)		1.11 (0.11)	No erosion		
Grote Houw	5	1,027	0.24	1	4.85 (0.38)	35							
Grote Houw	5	1,028	0.43	5	1.10 (0.25)	24	0.018 (0.004)						
Grote Houw	5	1,029	0.53	9	0.71 (0.12)	24	0.011 (0.002)						
Grote Houw	2	1,036	0.1	10	4.45 (0.15)	12	0.036 (0.001)	0.121 (0.012)		0.93 (0.09)	21.61 (26.81)	22.41 (30.31)	0.43–1.05
Grote Houw	2	1,037	0.28	11	4.98 (0.42)	19	0.063 (0.005)						
Grote Houw	2	1,038	0.4	12	1.75 (0.41)	19	0.022 (0.005)						
Grote Houw	1	1,046	0.09	13.1	5.06 (0.32)	14	0.047 (0.003)	0.098 (0.008)		0.75 (0.06)	73.83 (17.95)	84.51 (24.65)	1.12–2.18
Grote Houw	1	1,047	0.2	13.2	4.86 (0.41)	12	0.039 (0.003)						
Grote Houw	1	1,048	0.36	14	1.22 (0.15)	15	0.012 (0.001)						
Grote Houw	1	1,049	0.45	15	0.45 (0.29)	>	–						
Grote Houw	4	1,058	0.12	16.1	6.15 (0.17)	21	0.086 (0.002)	0.136 (0.004)		1.05 (0.03)	No erosion		
Grote Houw	4	1,059	0.27	16.2	6.29 (0.17)	12	0.050 (0.001)						
Grote Houw	4	1,060	0.4	19	0.64 (0.07)	>	–						
Kelmond	1	66	0.25		7.95 (0.38)	35	0.186 (0.009)	0.282 (0.036)	0.2189	1.29 (0.17)	No erosion		
Kelmond	1	56	0.5		1.53 (0.34)	45	0.046 (0.010)						
Kelmond	1	57	0.75		1.68 (0.57)	45	0.051 (0.017)						
Kelmond	1	58	1		0.63 (0.40)	**							
Kelmond	1	59	1.25		1.24 (0.44)	**							
Kelmond	1	60	1.5		0.63 (0.15)	**							
Kelmond	3	69	0.25		6.80 (0.60)	30	0.136 (0.012)	0.152 (0.013)		0.70 (0.06)	91.13 (17.79)	108.23 (26.49)	1.47–2.69
Kelmond	3	71	0.4		1.23 (0.08)	20	0.016 (0.001)						
Kelmond	4	76	0.25		8.79 (0.19)	30	0.176 (0.004)	0.222 (0.021)		1.02 (0.09)	No erosion		
Kelmond	4	77	0.4		1.62 (0.51)	20	0.022 (0.007)						
Kelmond	4	78	0.65		1.25 (0.50)	30	0.025 (0.010)						
Kelmond	4	79	0.85		0.61 (0.48)	**							
Meerssen	28	34	0.2		8.54 (0.55)	40	0.228 (0.015)	0.259 (0.028)	0.1719	1.50 (0.16)	No erosion		
Meerssen	28	35	0.4		1.27 (0.54)	20	0.017 (0.007)						
Meerssen	28	36	0.7		1.06 (0.47)	20	0.014 (0.006)						
Meerssen	28	37	1		0.21 (0.48)	**							
Meerssen	28	38	1.4		0.35 (0.41)	**							
Meerssen	28	39	1.6		0.83 (0.15)	**							
Meerssen	28	40	1.9		0.00 (0.46)	**							
Meerssen	28	41	2.1		0.92 (0.56)	**							
Meerssen	29	68	0.1		7.17 (0.44)	25	0.119 (0.007)	0.119 (0.009)		0.69 (0.05)	91.65 (15.89)	75.76 (91.65)	1.52–2.65
Meerssen	29	69	0.23		0.00 (0.51)	5	0.000 (0.002)						
Meerssen	30	63	0.1		6.38 (0.53)	30	0.128 (0.011)	0.138 (0.012)		0.80 (0.07)	59.75 (20.43)	39.32 (59.75)	0.79–1.86
Meerssen	30	64	0.24		1.51 (0.15)	10	0.010 (0.001)						

(Continues)

TABLE 3 (Continued)

Sites	Boring or pit nr.	Sample nr.	Sample depth (m)	Feature nr. (Grote Houw)	^{137}Cs (Bq/kg) (*SD*)	Thickness of feature or horizon (cm)	^{137}Cs total in feature or horizon (Bq)	^{137}Cs total in profile or core (Bq)	Average site (Bq)	^{137}Cs; ratio profile/site average	Erosion rate (mm/50 years, $n_t = 1$)	Erosion rate (mm/50 year, $n_t = 50$)	Yearly erosion (mm/year)
Grote Houw	3	1,013	0.25	1 + 4	0.07 (0.01)	31	0.0015 (0.0001)	0.0022 (0.0002)	0.0020	0.99 (0.08)	No erosion		
Grote Houw	3	1,014	0.41	2	0.08 (0.01)	12	0.0006 (0.0001)						
Grote Houw	3	1,015	0.5	3	0.00 (-)	20	0.000 (–)						
Grote Houw	3	1016	0.6	3	0.00 (-)	20							
Grote Houw	5	1,026	0.15	1	0.11 (0.01)	35	0.0023 (0.0001)	0.0023 (0.0001)		1.09 (0.06)	No erosion		
Grote Houw	5	1,027	0.26	1	0.09 (0.00)	35							
Grote Houw	5	1,028	0.4	5	0.00 (–)	24	0.000 (–)						
Grote Houw	5	1,029	0.55	9	0.00 (–)	24	0.000 (–)						
Grote Houw	2	1,036	0.1	10	0.08 (0.00)	12	0.006 (0.0000)	0.0015 (0.0001)		0.69 (0.03)	83.31 (10.08)	97.28 (14.19)	1.46–2.23
Grote Houw	2	1,037	0.28	11	0.07 (0.00)	19	0.009 (0.0000)						
Grote Houw	2	1,038	0.4	12	0.00 (–)	19	0.000 (–)						
Grote Houw	1	1,046	0.05	13.1	0.08 (0.00)	14	0.008 (0.0000)	0.0015 (0.0000)		0.73 (0.02)	74.66 (6.71)	85.60 (9.01)	1.36–1.89
Grote Houw	1	1,047	0.22	13.2	0.09 (0.00)	12	0.007 (0.0000)						
Grote Houw	1	1,048	0.33	14	0.00 (–)	15	0.000 (–)						
Grote Houw	1	1,049	0.45	15	0.00 (–)	>	–						
Grote Houw	4	1,058	0.05	16.1	0.12 (0.00)	21	0.0017 (0.0001)	0.0027 (0.0001)		1.26 (0.05)	No erosion		
Grote Houw	4	1,059	0.25	16.2	0.11 (0.01)	12	0.0009 (0.0000)						
Grote Houw	4	1,060	0.36	19	0.00 (–)	>							
Kelmond	1	66	0.25		0.16 (0.00)	35	0.0036 (0.0000)	0.0040 (0.0001)	0.0019	2.01 (0.05)	No erosion		
Kelmond	1	56	0.5		0.01 (0.00)	45	0.0003 (0.0001)						
Kelmond	1	57	0.75		0.00 (–)	45	0.000 (–)						
Kelmond	1	58	1		0.02 (0.00)	**							
Kelmond	1	59	1.25		0.00 (–)	**							
Kelmond	1	60	1.5		0.00 (–)	**							
Kelmond	3	69	0.25		0.03 (0.00)	30	0.0005 (0.0000)	0.0005 (0.0000)		0.26 (0.01)	219.81 (2.52)	390.65 (9.34)	4.18–8.00
Kelmond	3	71	0.4		0.00 (–)	20	0.000 (–)						
Kelmond	4	76	0.25		0.06 (0.00)	30	0.0011 (0.0001)	0.0013 (0.0001)		0.61 (0.01)	111.74 (4.04)	139.14 (6.44)	1.76–2.91
Kelmond	4	77	0.4		0.01 (0.00)	20	0.0001 (0.0000)						
Kelmond	4	78	0.65		0.00 (–)	30	0.000 (–)						
Kelmond	4	79	0.85		0.00 (–)	**							
Meerssen	28	34	0.2		0.16 (0.01)	40	0.0042 (0.0002)	0.0046 (0.0002)	0.0031	1.44 (0.06)	No erosion		
Meerssen	28	35	0.4		0.04 (0.00)	20	0.0005 (0.0000)						
Meerssen	28	36	0.7		0.00 (–)	20	0.000 (–)						
Meerssen	28	37	1		0.00 (–)	**							
Meerssen	28	38	1.4		0.00 (–)	**							
Meerssen	28	39	1.6		0.00 (–)	**							
Meerssen	28	40	1.9		0.00 (–)	**							
Meerssen	28	41	2.1		0.00 (–)	**							
Meerssen	29	68	0.1		0.13 (0.00)	25	0.0021 (0.0000)	0.0022 (0.0000)		0.69 (0.02)	88.06 (4.51)	103.88 (6.41)	1.67–2.21
Meerssen	29	69	0.23		0.01 (0.00)	5	0.0000 (0.0000)						
Meerssen	30	63	0.1		0.12 (0.00)	30	0.0023 (0.0001)	0.0024 (0.0001)		0.76 (0.04)	62.58 (10.86)	70.02 (13.97)	1.03–1.68
Meerssen	30	64	0.24		0.02 (0.00)	10	0.0000 (0.0000)						

uncertainties (see Table 1) suggesting that any impact of a possible fluctuation over time is not significant.

Thus, our data are not indicating a systematic bias in the initial disturbance ages caused by changing environmental dose rate conditions. In fact, the vast majority of initial disturbance, as well as stabilization ages, are in very good stratigraphic order (see Figures 4,6) and furthermore in line with the geological as well as archaeological interpretation, again supporting the validity of the OSL age interpretation.

It must be stressed that this may not be true in other environments: for example, in settings with very intensive mineral or clay leaching, desert pavements and thus trapping of aeolian dust (Fuchs & Lomax, 2018), or significant fluctuation of the ground water table (especially in combination with very fine-grained material).

4.3 | Cs and Pu results

A plot of ^{137}Cs versus $^{239+240}$Pu (Figure 7a) show that there is in general a correlation between the concentrations of these isotopes. Exceptions are the topsoil samples from Beek-Kelmond cores 3 and 4, which fall outside the correlation with higher Cs concentrations. Figure 7b shows that the ratio of the Pu isotopes generally falls within the range of 0.165–0.195.

Depth profiles of the fallout isotopes in Figures 4c, 5c, and 6c make clear that elevated concentrations can be found in the plow layer of all of the investigated locations. Where multiple samples are available from the plow layer—as in most of the Grote Houw test pits—their concentrations are very similar. There is a truncation below the plow layer.

4.4 | Cs and Pu interpretation

The ^{240}Pu/^{239}Pu isotope ratios of 0.165–0.195 are concordant with the stratospheric fallout and agree well with the benchmark ratios of 0.180 ±0.014 (2-sigma) cited in Kelley, Bond, and Beasley (1999) for northern Hemisphere, mid-latitude deposition. The Pu from the Chernobyl accident has an isotope ratio of ~0.4 (Ketterer & Szechenyi, 2008; Ketterer et al., 2004, Muramatsu et al., 2000) and our results demonstrate that any Chernobyl-derived impacts at the study locations are negligible compared to stratospheric fallout. The comparison between ^{137}Cs and $^{239+240}$Pu activities illustrates a dominance of 1950s–1960s fallout for both tracers at all sites, with the notable exception of Beek-Kelmond, where it appears that 1986 Chernobyl deposition is present in cores 3 and 4. Accordingly, we assumed the applicability of timeframes of 50–60 years for all $^{239+240}$Pu-based erosion estimates, and 30 years for the profiles with indicated dominant Chernobyl-derived ^{137}Cs contributions. (Wilkinson et al., 2006).

The above-0 values of ^{137}Cs in samples from below the plow layer may be background noise, especially since they also occur in older, deeply buried deposits. We cannot be certain of that in the horizons immediately below the plow layer, however, so these values are included in the calculations; they are indicated by colored bars in Figures 4–6c.

The calculation of the erosion rates is given in Table 3. Assuming erosion occurred within the investigated fields, and did not cross field boundaries, we used the average amount of fallout isotopes over all locations as $t = 0$ value to calculate erosion rates using Equation (3). The variation in erosion rates was determined by the confidence interval of the analyses (we took standard deviations for that) and by calculating the erosion rates for $n_t = 1$ and $n_t = 50$, that is assuming all erosion occurred in one event as well as assuming erosion occurred as yearly events. The results show that erosion is—as expected—strongest on the steepest parts of the slopes in Meerssen and Beek-Kelmond.

Average maximum erosion rates lie between 1.5 and 2 mm/year when ^{137}Cs is used, and between 2 and 6 when $^{239+240}$Pu is used. This may be simply due to variability within the method: Given a large number of uncertainties and assumptions, and the low amount of test locations (cores and profiles), the results of both methods come remarkably close. If there is a systematic difference, it may be caused by the stronger susceptibility of ^{137}Cs for leaching (Ibrahim & Morris, 1997; Tegen & Dörr, 1996; Yamamoto, Yamamori, Komura & Sakananoue, 1980).

5 | DISCUSSION

5.1 | Integrating OSL data and fallout isotopes

OSL ages inform on soil redistribution patterns at much larger timescales than the fallout isotopes. Combining both methods within profiles, as we did in the present project—makes it possible to test assumptions related to both methods: Ideally, the fallout isotope signal is restricted to the topsoil. Leaching and/or bioturbation may, however, affect their distribution in a soil profile as well. Bioturbation potentially also affects OSL, by transporting recently bleached grains downward, whereas leaching does not. Incomplete mixing in the (plowed) topsoil may, however, also play a role. This makes it very insightful to compare the depth profiles obtained by both methods.

Significant concentrations of Pu and Cs isotopes were detected in all topsoil samples, with recent ages confirmed by sub-recent OSL stabilization ages. However, all sites have at least one profile in which detectable (but often small) amounts of Pu and Cs isotopes were detected in samples where the bsMAM stabilization ages clearly predate the bomb tests, for example, Beek-Kelmond core 1 and 4 (OSL stabilization ages of 450 and ~1,500 years) and Meerssen core 30 (OSL stabilization age of ~1,200 years) and Grote Houw WP4 (OSL stabilization age ~600 years). This suggest that some leaching has occurred. Moreover, it seems that Pu is less sensitive to leaching than Cs (e.g., see core 4 of Beek-Kelmond or WP5 in Grote Houw). This would not only make Pu more advantageous as tracer for erosion studies because of its longer half-life, but also because of its lower sensitivity to leaching. Apart from these few overlaps, the two methods (fallout isotopes and OSL) provide mostly data on different timescales.

5.2 | OSL results and taphonomy

The depth plots of the single-aliquot OSL ages combined with the stabilization (bsMAM) and initial disturbance (FMM_{oldest}) age give a surprisingly well interpretable pattern in all three sites (see above). It clearly traces past sedimentary deposition, for example, loess deposition (in Beek-Kelmond core 1 samples 54 and 55 and Meerssen core 28, samples 33 and 32), tidal deposition (in the deepest samples in Grote Houw WP4 7WP5), and formation of colluvium (e.g., Beek-Kelmond core 1, samples 51 and 52; Meerssen core 28 samples 31–27). It indicates soil profiles that have been in a stable landscape position (e.g., Meerssen core 29, sample 67) and it helps identify hiatuses and sequences that have been affected by erosion (e.g., Beek-Kelmond core 3 and possibly Meerssen core 30). This makes this approach very suitable for studying erosion/sedimentation processes on slopes especially on decennial to millennia timescales, and as a tool for the taphonomical study on archaeological sites in erosive landscapes. For archaeological sites in accretionary landscapes, like the coastal floodplains of Grote Houw, the added value is yet less clear. Incomplete bleaching/mixing in the plow layers (at Grote Houw) results in highly scattered age distributions. This makes this approach not precise enough for determining recent erosion/deposition processes.

5.3 | Fall-out isotopes results and modern erosion

The stratospheric fallout isotopes ^{137}Cs and $^{239+240}$Pu appear to be useful tools for determining recent erosion rates on annual to decadal scales. In particular, the present study underscores the versatility of $^{239+240}$Pu as a powerful tracer with a better-known time of origin than is possible with a mixture of ^{137}Cs of 1950–1960 stratospheric fallout versus 1986 Chernobyl source terms. If erosion rate estimates are determined using ^{137}Cs distributions only, for sites from many areas of Europe, it remains ambiguous as to whether the erosion reference ($t = 0$) time corresponds to the 1950–1960 versus 1986. The thickness of the (fallout bearing) plow layer is an important factor in the erosion calculation: After all, the total amount of fallout isotopes is calculated from layer thicknesses and concentrations. Still, we need the isotopes to confirm that these erosion processes occurred quite recently rather than centuries ago.

5.4 | Implications

The three investigated sites have different ages and formation histories and occur in two fundamentally different landscape types. What they have in common is that the archaeological remains probably occur at surface level to depths of at least 1 m; plus each site is threatened by ongoing soil erosion. If unchecked, this process will result in the redistribution of near-surface artifacts eventually destroying spatial context and the integrity of archaeological finds as well as the gradual taking up of more and more anthropogenic features into the plow layer. The latter is the more damaging, as it irrevocably prohibits any future research or recording of these features and their relation with the artifact present in the site. The most effective way of preventing such damage is probably to stop plowing and turn the fields into grassland or similar permanent vegetation.

6 | CONCLUSIONS

On archaeological sites that are susceptible to erosion, depth plots of small single-aliquot OSL ages can be used to derive the taphonomical history of the site and to identify erosive, stable and accreting landscape elements. For more recent erosion processes, however, where annual to decadal dating resolution is required, incomplete bleaching and mixing of sediment in the plow layer prevent reliable dating of erosion events.

A combination of the fallout isotopes ^{137}Cs and $^{239+240}$Pu, however, did give insights into more recent erosion processes of the past several decades. The ^{240}Pu/^{239}Pu atom ratios confirmed the stratospheric fallout origin of this tracer, indicating that the measured erosion is interpreted as taking place since the 1950–1960 deposition of stratospheric fallout. Calculated erosion rates from ^{137}Cs and $^{239+240}$Pu on plowed lands averaged 2–6 mm/year on the sites investigated. Of the two fallout tracers used, Pu isotopes appear less sensitive to leaching.

ACKNOWLEDGMENTS

Thanks are due to the landowners and farmers who gave permission to access their land. The use of the TNO facilities to open, describe, and sample the cores is greatly appreciated. Wim Jong and Mario van IJzendoorn supported the fieldwork and sampling. Willem Derickx prepared the maps in Figures 4–6a,b. Two anonymous reviewers are thanked for their comments that helped improve this publication. This study was part of the TOPsites project, funded by the Ministry of Education, Culture and Science.

ORCID

Hans Huisman http://orcid.org/0000-0002-4742-536X

REFERENCES

Aitken, M. J. (1985). *Thermoluminescence dating* (US ed.). London: Academic press.

Alewell, C., Meusburger, K., Juretzko, G., Mabit, L., & Ketterer, M. E. (2014). Suitability of $^{239+240}$Pu and $_{137}$Cs as tracers for soil erosion assessment in mountain grasslands. *Chemosphere*, *103*, 274–280.

Alewell, C., Pitois, A., Meusburger, K., Ketterer, M., & Mabit, L. (2017). $^{239+240}$Pu form "contaminant" to soil erosion tracer: Where do we stand? *Earth-Science Reviews*, *172*, 107–123.

Arnold, L. J., & Roberts, R. G. (2009). Stochastic modelling of multi-grain equivalent dose (De) distributions: Implications for OSL dating of sediment mixtures. *Quaternary Geochronology*, *4*(3), 204–230.

Baartman, J. E. M., Temme, A. J. A. M., Schoorl, J. M., Braakhekke, M. H. A., & Veldkamp, T. A. (2012). Did tillage erosion play a role in millennial

scale landscape development? *Earth Surface Processes and Landforms*, *37*(15), 1615–1626.

Bateman, M. D., Frederick, C. D., Jaiswal, M. K., & Singhvi, A. K. (2003). Investigations into the potential effects of pedoturbation on luminescence dating. *Quaternary Science Reviews*, *22*, 1169–1176.

Behm, H. A., Bräuning, A., Ende, F., Hartsch, K., Schmidt, W.-A., Strobel, M. … Westphalen, Th. (2011). *Archäologie und Landwirtschaft*. Osnabrück: Deutsche Bundesstiftung Umwelt.

Bennett, B. G. (2002). Worldwide dispersion and deposition of radionuclides produced in atmospheric tests. *Health Physics*, *82*, 644–655.

Brounen, F. T. S., & Rensink, E. (2007). *Kelmond-Beekerveld (gemeente Beek). Waardestellend onderzoek van een omgrachte nederzetting uit het Vroeg-Neolithicum A (Lineaire Bandkeramiek), Rapportage Archeologische Monumentenzorg 153*. Amersfoort: Cultural Heritage Agency of the Netherlands.

Council of Europe (1992). European convention on the protection of the archaeological heritage (revised), European Treaty Series No. 143.

Cultural Heritage Agency (2016). Bulletin of acts orders and decrees of the kingdom of the Netherlands, 511, pp. 1–57.

Cunningham, A. C., & Wallinga, J. (2010). Selection of integration time intervals for quartz OSL decay curves. *Quaternary Geochronology*, *5*(6), 657–666.

Diez-Martín, F. (2010). Evaluating the effect of plowing on the archaeological record: The early middle palaeolithic in the river Duero basin plateaus (north-central Spain). *Quaternary International*, *214*(1-2), 30–43.

Dreibrodt, S., Jarecki, H., Lubos, C., Khamnueva, S. V., Klamm, M., & Bork, H.-R. (2013). Holocene soil formation and soil erosion at a slope beneath the Neolithic earthwork Salzmünde (Saxony-Anhalt, Germany). *Catena*, *107*, 1–14.

Fuchs, M., & Lang, A. (2009). Luminescence dating of hillslope deposits—A review. *Geomorphology*, *109*(1-2), 17–26.

Fuchs, M., & Lomax, J. (2018). Stone pavements in arid environments: Reasons for D_e overdispersion and grain-size dependent OSL ages. *Quaternary Geochronology*. https://doi.org/10.1016/j.quageo.2018.05.013

Gaspar, L., Navas, A., Walling, D. E., Machín, J., & Gómez Arozamena, J. (2013). Using ^{137}Cs and ^{210}Pb to assess soil redistribution on slopes at different temporal scales. *Catena*, *102*, 46–54.

Govers, G., Vandaele, K., Desmet, P., Poesen, J., & Bunte, K. (1994). The role of tillage in soil redistribution on hillslopes. *European Journal of Soil Science*, *45*, 469–478.

de Groot, T. (2005). *De Romeinse villa Meerssen-Onderste Herkenberg, Rapportage Archeologische Monumentenzorg 125*. Amersfoort: ROB.

Govers, G., Vandaele, K., Desmet, P., Poesen, J., & Bunte, K. (2011). Dose-rate conversion factors: Update. *Ancient TL*, *29*(1), 5–8.

Huisman, D. J., de Groot, T., & de Kort, J. W. (2017). Huisman, D. J., de Groot, T., & de Kort, J. W. (Eds.), *Meerssen-Onderste Herkenberg; Erosieonderzoek in het kader van TOPsites, Rapportage Archeologische Monumentenzorg (RAM) 239*. Amersfoort: Cultural Heritage Agency of the Netherlands. Retrieved from. https://cultureelerfgoed.nl/sites/default/files/publications/ram-239_meerssen-onderste_herkenberg_0.pdf

Huisman, D. J., & de Kort, J. W. (Eds.), 2017). *Kelmond-Beekerveld (gemeente Beek); erosieonderzoek in het kader van het TOPsites project, Rapportage Archeologische Monumentenzorg (RAM) 237*. Amersfoort: Cultural Heritage Agency of the Netherlands. Retrieved from. https://cultureelerfgoed.nl/sites/default/files/publications/ram-237_kelmond-bleekerveld_erosieonderzoek_0.pdf

Huisman, D. J., van der Heiden, M., Derickx, W., de Kort, J. W., Reimann, T., Schoorl, J., … Wallinga, J. (2017). *Erosie-onderzoek op de Grote Houw Oost in het kader van TOPsites, Rapportage Archeologische Monumentenzorg (RAM) 238*. Amersfoort: Cultural Heritage Agency of the Netherlands. Retrieved from. https://cultureelerfgoed.nl/sites/default/files/publications/ram-238_grote_houw.pdf

Huisman, H., & van Os, B. (2016). Relax don't do it: A future for archaeological monitoring. *Conservation and Management of Archaeological sites*, *18*, 372–386.

Ibrahim, S. A., & Morris, R. C. (1997). Distribution of plutonium among soil phases near a Subsurface Disposal area in Southeastern Idaho, USA. *Journal of Radioanalytical and Nuclear Chemistry*, *226*(1-2), 217–220.

Kachanoski, R. G. (1993). Estimating soil loss from changes in soil ^{137}Cs. *Canadian Journal of Soil Science*, *73*, 629–632.

Kelley, J. M., Bond, L. A., & Beasley, T. M. (1999). Global distribution of Pu isotopes and ^{237}Np. *Science of the Total Environment*, *237/238*, 483–500.

Ketterer, M. E., Hafer, K. M., Jones, V. J., & Appleby, P. G. (2004). Rapid dating of recent sediments in Loch Ness: Inductively coupled plasma mass spectrometric measurements of global fallout plutonium. *Science of the Total Environment*, *322*(1-3), 221–229.

Ketterer, M. E., Hafer, K. M., & Mietelski, J. W. (2004). Resolving Chernobyl vs. global fallout contributions in soils from Poland using plutonium atom ratios measured by inductively coupled plasma mass spectrometry. *Journal of Environmental Radioactivity*, *73*, 183–201.

Ketterer, M. E., & Szechenyi, S. C. (2008). Determination of plutonium and other transuranic elements by inductively coupled plasma mass spectrometry: A historical perspective and new frontiers in the environmental sciences. *Spectrochimica Acta, Part B: Atomic Spectroscopy*, *63*(7), 719–737.

Ketterer, M. E., Zheng, J., & Yamada, M. (2012). Applications of transuranics as tracers and chronometers in the environment. In Baskaran, M. (Ed.), *Handbook of environmental isotope geochemistry* (pp. 395–417). Berlin.

Landschapsbeheer Groningen (1995). *Wierden voor het voetlicht*. Groningen: Landschapsbeheer Groningen.

Lüthgens, C., Böse, M., & Preusser, F. (2011). Age of the Pomeranian ice marginal position in north-eastern Germany determined by Optically Stimulated Luminescence (OSL) dating of glaciofluvial (sandur) sediments. *Boreas*, *40*, 598–615.

Madsen, A. T., Murray, A. S., Andersen, T. J., Pejrup, M., & Breuning-Madsen, H. (2005). Optically stimulated luminescence dating of young estuarine sediments: A comparison with ^{210}Pb and ^{137}Cs dating. *Marine Geology*, *214*, 251–268.

Mietelski, J. W., & Was, B. (1995). Plutonium from Chernobyl in Poland. *Applied Radiation and Isotopes*, *46*, 1203–1211.

Muramatsu, Y., Rühm, W., Yoshida, S., Tagami, K., Uchida, S., & Wirth, E. (2000). Concentrations of ^{239}Pu and ^{240}Pu and their isotopic ratios determined by ICP-MS in soils from the Chernobyl 30-km Zone. *Environmental Science and Technology*, *34*, 2913–2917.

Murray, A. S., & Wintle, A. G. (2003). The single-aliquot regenerative-dose protocol: Potential for improvements in reliability. *Radiation Measurements*, *37*, 377–381.

NEN (2009). *Nederlandse norm Radioactiviteitsmetingen; Monstervoorbewerking*. Delft: Nederlands Normalisatie Instituut. 7pp.

Olson, K. R., Gennadiyev, A. N., Zhidkin, A. P., Markelov, M. V., Golosov, V. N., & Lang, J. M. (2013). Use of magnetic tracer and radio-cesium methods to determine past cropland soil erosion amounts and rates. *Catena*, *104*, 103–110.

van Os, B. J. H., & Kosian, M. (2011). Sluipende degradatie van het archeologisch erfgoed. In Lauwerier, R. G. C. M., de Groot, T., van Os, B. J. H., & Theuninssen, L. (Eds.), *Vragen over Malta, Onderzoek naar de effectiviteit van de onderzoeksketen, sluipende degradatie en de effecten van vrijstelling, Rapportage Archaeologische Monumentenzorg (RAM) 196* (pp. 41–84). Amersfoort: Rijksdienst voor het Cultureelerfgoed. Retrieved from. https://cultureelerfgoed.nl/sites/default/files/publications/ram196-vragen-over-malta.pdf

Poesen, J., Wesemael, B., Govers, G., Martinez Fernandez, J., Desmet, P., Vandaele, K., … Degraer, G. (1997). Patterns of rock fragment cover generated by tillage erosion. *Geomorphology*, *18*, 183–197.

Poręba, G., & Bluszcz, A. (2008). Influence of the parameters of models used to calculate soil erosion based in ^{137}Cs tracer. *Geochronometria*, *32*, 21–27.

Prescott, J. R., & Hutton, J. T. (1994). Cosmic ray contributions to dose rates for luminescence and ESR dating: Large depths and long-term time variations. *Radiation Measurements*, *23*(2/3), 497–500.

Quine, T. A. (1999). Use of ^{137}Cs data for validation of spatially distributed erosion models: The implications of tillage erosion. *Catena*, *37*, 415–430.

Quine, T. A., Govers, G., Walling, D. E., Zhang, X., Desmet, P. J. J., Zhang, Y., & Vandaele, K. (1997). Erosion processes and landform evolution on agricultural land: New perspectives from Caesium-137 measurements and topographic based erosion modelling. *Earth Surface Processes and Landforms*, *22*, 799–816.

Reimann, T., Lindhorst, S., Thomsen, K. J., Murray, A. S., & Frechen, M. (2012). OSL dating of mixed coastal sediment (Sylt, German Bight, North Sea). *Quaternary Geochronology*, *11*, 52–67.

Reimann, T., Román-Sánchez, A., Vanwalleghem, T., & Wallinga, J. (2017). Getting a grip on soil reworking – Single-grain feldspar luminescence as a novel tool to quantify soil reworking rates. *Quaternary Geochronology*, *42*, 1–14.

Ritchie, J. C., & McHenry, J. R. (1990). Application of radioactive fallout cesium-137 to measuring soil erosion and sediment accumulation rates and patterns: A review. *Journal of Environmental Quality*, *19*, 215–233.

Roberts, R. G., Jacobs, Z., Li, B., Jankowski, N. R., Cunningham, A. C., & Rosenfeld, A. B. (2015). Optical dating in archaeology: Thirty years in retrospect and grand challenges for the future. *Journal of Archaeological Science*, *56*, 41–60.

Schoorl, J. M., Boix Fayos, C., de Meijer, R. J., van der Graaf, E. R., & Veldkamp, A. (2004). The 137Cs technique applied to steep Mediterranean slopes (Part II): Landscape evolution and model calibration. *Catena*, *57*(1), 35–54.

Stoutjesdijk, J. F. (1986). *De radioactieve besmetting in Nederland ten gevolge van het kernreactorongeval in Tsjernobyl. Coordinatie-commissie voor de metingen van radioactiviteit en Xenobiotischestoffen*. Bilthoven: RIVM.

Tegen, I., & Dörr, H. (1996). Mobilization of cesium in organic rich soils: Correlation with production of dissolved organic carbon. *Water, Air, and Soil Pollution*, *88*, 133–144.

Walling, D. E., Collins, A. L., & Sichingabula, H. M. (2003). Using unsupported lead-210 measurements to investigate soil erosion and sediment delivery in a small Zambian catchment. *Geomorphology*, *25*(3-4), 193–213.

Walling, D. E., & Quine, T. A. (1990). Calibration of ^{137}Cs measurements to provide quantitative erosion rate data. *Land Degradation and Rehabilitation*, *2*, 161–175.

Walling, D. E., & Quine, T. A. (1991). Use of ^{137}Cs measurements to investigate soil erosion on arable fields in the UK: Potential applications and limitations. *Journal of Soil Science*, *42*, 147–165.

Walling, D. E., & Quine, T. A. (1992). The use of ^{137}Cs measurements in soil erosion surveys. In Bogen, J., Walling, D. E., & Day, T. J. (Eds.), *Erosion and sediment transport monitoring programmes in river Basins (Proceedings of the Oslo Symposium, August 1992* (pp. 143–153). IAHS Publication No. 210, Wallingford, UK.

Wilkinson, K., Tyler, A., Davidson, D., & Grieve, I. (2006). Quantifying the threat to archaeological sites from the erosion of cultivated soil. *Antiquity*, *80*, 658–670.

Yamamoto, M., Yamamori, S., Komura, K., & Sakanoue, M. (1980). Behavior of plutonium and americum in soils. *Journal of Radiation Research*, *21*(3-4), 204–212.

Zhang, X., Higgitt, D. L., & Walling, D. E. (1990). A preliminary assessment of the potential for using ^{137}Cs to estimate rates of soil erosion in the Loess Plateau of China. *Hydrological Sciences Journal*, *35*, 243–252.

Zhang, X., Quine, T. A., & Walling, D. E. (1998). Soil erosion rates on sloping cultivated land on the Loess Plateau near Ansai, Shaanxi Province, China: An investigation using ^{137}Cs and rill measurements. *Hydrological Processes.*, *12*, 171–189.

How to cite this article: Huisman H, de Kort J-W, Ketterer ME, et al. Erosion of archaeological sites: Quantifying the threat using optically stimulated luminescence and fallout isotopes. *Geoarchaeology*. 2019;34:478–494.
https://doi.org/10.1002/gea.21716